# Glyphs for Asymmetric Second-Order 2D Tensors

Nicholas Seltzer and Gordon Kindlmann

Department of Computer Science and Computation Institute, University of Chicago, USA

## Abstract

*Tensors model a wide range of physical phenomena. While symmetric tensors are sufficient for some applications (such as diffusion), asymmetric tensors are required, for example, to describe differential properties of fluid flow. Glyphs permit inspecting individual tensor values, but existing tensor glyphs are fully defined only for symmetric tensors. We propose a glyph to visualize asymmetric second-order two-dimensional tensors. The glyph includes visual encoding for physically significant attributes of the tensor, including rotation, anisotropic stretching, and isotropic dilation. Our glyph design conserves the symmetry and continuity properties of the underlying tensor, in that transformations of a tensor (such as rotation or negation) correspond to analogous transformations of the glyph. We show results with synthetic data from computational fluid dynamics.*

Categories and Subject Descriptors (according to ACM CCS):   Computer Graphics [I.3.5]: Curve, surface, solid, and object representations—Computer Graphics [I.3.8]: Applications—

## 1. Introduction

Tensors provide an essential mathematical model for a range of physical phenomena. Some important examples are in physics (stress/strain, deformation gradient, velocity gradient), biomedicine (diffusion), geometry (metric/curvature), and computer vision (structure). For many applications, the problem of analyzing or visualizing the tensor field is simplified by the tensor being symmetric ($\mathbf{T^t} = \mathbf{T}$). Other tensors, such as from deformation and velocity gradients, are not symmetric.

Though there has been significant work on asymmetric tensor field analysis, the community lacks an established method for visualizing the tensor itself, even in the two-dimensional case. We focus on exactly this problem. Glyphs are an ideal visualization choice for displaying tensors at discrete points, since the glyph shape, orientation, and appearance encode all the degrees of freedom in the tensor.

This paper proposes a glyph for visualizing general two-dimensional second-order tensors. There are several design principles we hope to follow. We want the design to be continuous and disambiguous: tensors that are very similar should be represented with visually similar glyphs and tensors that are very different should be visually distinct. The glyph should preserve the symmetries of the tensor: if the tensor is symmetric to some change in coordinates (e.g. a rotation), the glyph should exhibit a similar symmetry.

Tensor decomposition often plays a fundamental role in tensor analysis. There are different ways to decompose a tensor, and the most informative decomposition may be application dependent. We

hope to make several basic tensor properties easily identifiable from the glyph appearance: the isotropic, deviatoric, and rotational components, and the properties of the tensor eigensystem.

Our main contribution is a new tensor glyph (Sec. 4), modestly expanding the class of tensors with fully defined glyphs to asymmetric 2D 2nd-order tensors (i.e., $2 \times 2$ matrices). We make sure to include previous tensor glyphs as special cases of our own, and we demonstrate that algebraic visualization design [KS14] can constructively guide each step of constructing a new visual encoding. Our design is created within a novel barycentric space to organize unit-norm tensors. Our glyph definition benefits from revisiting (Sec. 3) the mathematical bases of previous work with asymmetric tensors [ZP05, ZYLL09, CPL*11]. Our contributions here include clarifications of which tensor decomposition coordinates are invariant with respect to basis, and expressions of (dual,pseudo)eigenvectors simplified by exploiting double angle formulae to parameterize tensor orientation.

## 2. Background and Related Work

### 2.1. Tensor Field Visualization

Existing methods for tensor field visualization fall into several categories; surveys [LV12, KASH13] provide more context. Some direct methods use color-mapping and volume rendering [DGBW09, KWH00] to depict large, continuous regions. Other methods that produce dense visualizations of continuous regions of the field include texture-based methods like LIC and brush-strokes [LAK*98, ZP03, HFH*04].

Geometry-based methods create shapes that encode tensor properties. Glyphs are small shapes used to represent individual tensors at particular locations in the field (more in section 2.2). Hyperstreamlines [DH93] and hyperstreamsurfaces [JSF*02] are lines and surfaces that follow the eigenvectors of the tensor field in a method similar to streamlines in vector field visualization (topological skeletons being a special case of hyperstreamlines [HLL97]). These methods are also sometimes combined to create hybrid visualizations [ZYLL09]. Continuous renderings can be used to provide context for glyphs or other geometry based methods [SEHW02, DGBW09].

## 2.2. Tensor glyphs

For symmetric tensors, our glyphs are very similar to existing superquadric glyphs [SK10b]. These glyphs are scaled and rotated to match the scaling and orientation of the eigensystem of the tensor. We extend the design to apply to asymmetric tensors as well, representing asymmetric glyphs by more complex deformations to the base shape. Other shapes have also been used for the base geometry of tensor glyphs, including of unit spheres [BML94], cylinders [WLW00], and multiple superimposed shapes [Hab90, WMK*99]. Often these shapes are deformed by scaling and rotating the glyph so the axes are aligned with the eigenvectors of the tensor and the dimensions match the eigenvalues. A different approach is to create planes [NJP05] or more complex analytic surfaces representing tensor properties [MSM95, HYW03].

A lot of existing work visualizing asymmetric tensor fields is specifically motivated by vector field analysis, with many placing special emphasis on using glyphs to represent the Jacobian near critical points of the field. Field lines near such critical points are one source of inspiration for our glyph shape. Several other works already closely match streamline shapes, including the concave superquadrics for indefinite tensors [SK10b] and the elliptical glyphs representing tensors with complex eigensystems [CPL*11]. There are other methods for visualizing vector fields which incorporate features of the Jacobian [dLvW93, AKK*13, TWHS03] into the visualization, but do not apply to the visualization of tensor fields alone.

Aside from shape, color is another important consideration for glyph design. Two common techniques are to use color to indicate eigenvalue sign [Hab90, JSF*02, SK10a] or eigenvector orientation [WLW00]. In general, color is well used to differentiate properties of the tensor that are unclear from the shape of the glyph alone.

## 3. Tensor Algebra

The following decomposition and parameterization of the space of second-order two-dimensional tensors underlies the design space of our new glyphs. Instead of using tensor invariants, as in previous tensor glyph designs [SK10b], we define our space in terms of the $2 \times 2$ matrix $\mathbf{T}$ representing a tensor *in a given orthonormal basis* for $\mathbb{R}^2$, and note invariances with respect to the basis as they arise.

Following previous work [ZYLL09, CPL*11], we decompose $\mathbf{T}$ into isotropic $\mathbf{C}_D$, traceless symmetric (deviatoric) $\mathbf{C}_S$, and anti-

symmetric $\mathbf{C}_R$ components, via

$$\mathbf{T} = \underbrace{\tfrac{1}{2}(\mathbf{T}+\mathbf{T}^t)}_{\text{(symmetric)}} + \underbrace{\tfrac{1}{2}(\mathbf{T}-\mathbf{T}^t)}_{\text{(antisymmetric)}} \tag{1}$$

$$= \underbrace{\tfrac{1}{2}\operatorname{tr}(\mathbf{T})\mathbf{I}}_{=\mathbf{C}_D} + \underbrace{\tfrac{1}{2}(\mathbf{T}+\mathbf{T}^t) - \tfrac{1}{2}\operatorname{tr}(\mathbf{T})\mathbf{I}}_{=\mathbf{C}_S} + \underbrace{\tfrac{1}{2}(\mathbf{T}-\mathbf{T}^t)}_{=\mathbf{C}_R} \tag{2}$$

$\mathbf{T}^t$ and $\operatorname{tr}(\mathbf{T})$ are the transpose and trace of $\mathbf{T}$; using these operations ensures that the decomposition is invariant with respect to basis. The $\mathbf{C}_D$, $\mathbf{C}_S$, $\mathbf{C}_R$ components capture three basic modes of fluid parcel motion: isotropic expansion, anisotropic stretching, and rotation, respectively. This decomposition is common in fluid dynamics [Bat67] and particularly in the previous work on visualizing velocity gradients [ZYLL09, CPL*11].

How we parameterize these three components is functionally equivalent to previous work, though we clarify here relationships between invariants, bases, and eigenvector orientation. We define basis *matrices* to span the isotropic, traceless symmetric, and antisymmetric subspaces:

$$\mathbf{B}_D = \tfrac{1}{\sqrt{2}}\begin{bmatrix} 1 & 0 \\ 0 & 1 \end{bmatrix} \quad \mathbf{B}_R = \tfrac{1}{\sqrt{2}}\begin{bmatrix} 0 & -1 \\ 1 & 0 \end{bmatrix}$$
$$\mathbf{B}_{S_1} = \tfrac{1}{\sqrt{2}}\begin{bmatrix} 1 & 0 \\ 0 & -1 \end{bmatrix} \quad \mathbf{B}_{S_2} = \tfrac{1}{\sqrt{2}}\begin{bmatrix} 0 & 1 \\ 1 & 0 \end{bmatrix}. \tag{3}$$

The decomposition (2) can be stated in this basis as:

$$\mathbf{T} = \underbrace{D(\mathbf{T})\mathbf{B}_D}_{=\mathbf{C}_D} + \underbrace{S_1(\mathbf{T})\mathbf{B}_{S_1} + S_2(\mathbf{T})\mathbf{B}_{S_2}}_{=\mathbf{C}_S} + \underbrace{R(\mathbf{T})\mathbf{B}_R}_{=\mathbf{C}_R}; \tag{4}$$

$$X(\mathbf{T}) = X = \mathbf{T} : \mathbf{B}_X; \qquad X \in \{D, S_1, S_2, R\} \tag{5}$$

where ":" is the Frobenius inner product $\mathbf{A} : \mathbf{B} = \operatorname{tr}(\mathbf{A}\mathbf{B}^t)$. A change of basis between any two orthonormal bases for $\mathbb{R}^2$ is a unitary transform $\mathbf{T}' = \mathbf{Q}\mathbf{T}\mathbf{Q}^t$ where $\mathbf{Q}$ is a unitary matrix: $\mathbf{Q}^{-1} = \mathbf{Q}^t$ and $\det(\mathbf{Q}) = \pm 1$. The Frobenius inner product and norm $\|\mathbf{T}\|_F = \sqrt{\mathbf{T} : \mathbf{T}}$ are unitarily invariant (invariant under unitary transforms)[†]. In this sense $(\mathbf{B}_D, \mathbf{B}_{S_1}, \mathbf{B}_{S_2}, \mathbf{B}_R)$ is an orthonormal basis for $2 \times 2$ matrices, as is the standard ($\begin{bmatrix} 1 & 0 \\ 0 & 0 \end{bmatrix}, \begin{bmatrix} 0 & 1 \\ 0 & 0 \end{bmatrix}, \begin{bmatrix} 0 & 0 \\ 1 & 0 \end{bmatrix}, \begin{bmatrix} 0 & 0 \\ 0 & 1 \end{bmatrix}$) basis. We can reason about matrix $\mathbf{T}$ both as a linear transform and as a 4-vector. For example, the Frobenius norm $\|\mathbf{T}\|_F$ is the 4-vector length, computable in either matrix basis:

$$\mathbf{T} = \begin{bmatrix} a & b \\ c & d \end{bmatrix} \Rightarrow \|\mathbf{T}\|_F = \sqrt{a^2 + b^2 + c^2 + d^2} \tag{6}$$

$$= \sqrt{D^2 + S_1^2 + S_2^2 + R^2} \tag{7}$$

The isotropic component $\mathbf{C}_D$ is measured by the coordinate $D(\mathbf{T}) = \mathbf{T} : \mathbf{B}_D = \tfrac{1}{\sqrt{2}}\operatorname{tr}(\mathbf{T})$, which, being proportional to the trace, is the same in *any* $\mathbb{R}^2$ basis. The rotation component $\mathbf{C}_R$ is measured by $R(\mathbf{T}) = \mathbf{T} : \mathbf{B}_R$. $R(\mathbf{T})$ is unitarily invariant *up to sign*: one can show $R(\mathbf{T}') = R(\mathbf{Q}\mathbf{T}\mathbf{Q}^t) = -R(\mathbf{T})$ if $\det(\mathbf{Q}) = -1$ (i.e. $\mathbf{Q}$ rotates and reflects) and $R(\mathbf{T}') = R(\mathbf{T})$ if $\det(\mathbf{Q}) = 1$ ($\mathbf{Q}$ only rotates). We measure the remaining component $\mathbf{C}_S$ by its Frobenius norm.

---

[†] Note that unlike trace or determinant, the Frobenius norm is not invariant under all similarity transforms (arbitrary changes of basis).

By (4), (7), and the Pythagorean theorem,

$$S(\mathbf{T}) = \|\mathbf{T} - \mathbf{C}_D - \mathbf{C}_R\|_F = \|\mathbf{C}_S\|_F = \sqrt{S_1^2 + S_2^2} \qquad (8)$$

where $S_i = \mathbf{T} : \mathbf{B}_{S_i}$. $S(\mathbf{T})$ is unitarily invariant. While $D$ and $R$ are signed, $S$ is necessarily non-negative. The $D$, $S$, $R$ coordinates of $\mathbf{T}$ quantify the amounts in $\mathbf{T}$ of isotropic scaling, anisotropic stretching, and rotation, respectively [ZYLL09, CPL*11]. In terms of the elements of $\mathbf{T} = \begin{bmatrix} a & b \\ c & d \end{bmatrix}$,

$$D = \frac{a+d}{\sqrt{2}}; \ S = \frac{\sqrt{(a-d)^2 + (b+c)^2}}{\sqrt{2}}; \ R = \frac{c-b}{\sqrt{2}}. \qquad (9)$$

The final degree of freedom in $\mathbf{T}$ is the relationship between $S_1$ and $S_2$, parameterized by angle $\alpha \in [-\pi/2, \pi/2]$:

$$\tan(2\alpha) = \frac{S_2}{S_1} \ \Rightarrow \ \alpha = \tfrac{1}{2}\tan^{-1}(\tfrac{S_2}{S_1}) = \tfrac{1}{2}\tan^{-1}(\tfrac{b+c}{a-d}) \qquad (10)$$

The 2 factor in (10) is motivated by considering the double angle formulae and the standard 2D rotation matrix

$$\mathbf{A}(\alpha) = \begin{bmatrix} \cos\alpha & -\sin\alpha \\ \sin\alpha & \cos\alpha \end{bmatrix}, \qquad (11)$$

so that with (3) and (4):

$$\mathbf{C}_S = \frac{1}{\sqrt{2}} \begin{bmatrix} S_1 & S_2 \\ S_2 & -S_1 \end{bmatrix} = \frac{S}{\sqrt{2}} \begin{bmatrix} S_1/S & S_2/S \\ S_2/S & -S_1/S \end{bmatrix} \qquad (12)$$

$$= \frac{S}{\sqrt{2}} \begin{bmatrix} \cos 2\alpha & \sin 2\alpha \\ \sin 2\alpha & -\cos 2\alpha \end{bmatrix} = \frac{S}{\sqrt{2}} \begin{bmatrix} \cos^2\alpha - \sin^2\alpha & 2\sin\alpha\cos\alpha \\ 2\sin\alpha\cos\alpha & \sin^2\alpha - \cos^2\alpha \end{bmatrix} \qquad (13)$$

$$= \frac{S}{\sqrt{2}} \begin{bmatrix} \cos\alpha & -\sin\alpha \\ \sin\alpha & \cos\alpha \end{bmatrix} \begin{bmatrix} 1 & 0 \\ 0 & -1 \end{bmatrix} \begin{bmatrix} \cos\alpha & \sin\alpha \\ -\sin\alpha & \cos\alpha \end{bmatrix} \qquad (14)$$

$$= S\mathbf{A}(\alpha)\mathbf{B}_{S_1}\mathbf{A}(-\alpha) = S\mathbf{A}(\alpha)\mathbf{B}_{S_1}\mathbf{A}(\alpha)^{\mathsf{t}}. \qquad (15)$$

Eq. (14) diagonalizes $\mathbf{C}_S$, so eigenvectors of $\mathbf{C}_S$ are rows of $\mathbf{A}(-\alpha)$ or columns of $\mathbf{A}(\alpha)$: $\begin{bmatrix} \cos\alpha \\ \sin\alpha \end{bmatrix} = \mathbf{A}(\alpha)\begin{bmatrix} 1 \\ 0 \end{bmatrix}$ and $\begin{bmatrix} -\sin\alpha \\ \cos\alpha \end{bmatrix} = \mathbf{A}(\alpha)\begin{bmatrix} 0 \\ 1 \end{bmatrix}$, with eigenvalues $\pm S/\sqrt{2}$. Our contribution is using the double angle formulae to express $\mathbf{C}_S$ in terms of $\alpha$ rather than $\theta = 2\alpha \in [-\pi, \pi]$ [ZYLL09, CPL*11][‡]. This naturally parameterizes the orientation, relative to the given $\mathbb{R}^2$ basis, of both $\mathbf{C}_S$ and (since $\mathbf{C}_D$ and $\mathbf{C}_R$ are rotationally symmetric) $\mathbf{T}$ itself. One can similarly show

$$\mathbf{B}_{S_2} = \mathbf{A}(\pi/4)\mathbf{B}_{S_1}\mathbf{A}(-\pi/4), \qquad (16)$$

i.e., the $\mathbf{B}_{S_1}$ and $\mathbf{B}_{S_2}$ basis matrices capture the same deformation, but along different directions (they are rotations of each other), and the orientation of $\mathbf{T}$ is entirely determined by how it projects onto $\mathbf{B}_{S_1}$ and $\mathbf{B}_{S_2}$, using (5).

Summarizing (4), (11), and (15), we reconstitute $\mathbf{T}$ from its $(D, S, R, \alpha)$ coordinates by:

$$\mathbf{T} = \mathbf{M}(D, S, R, \alpha) = D\mathbf{B}_D + S\mathbf{A}(\alpha)\mathbf{B}_{S_1}\mathbf{A}(\alpha)^{\mathsf{t}} + R\mathbf{B}_R \qquad (17)$$

Formulae for invariants of $\mathbf{T}$ can be found by setting

$$\alpha = 0 \Rightarrow \mathbf{A}(\alpha) = \mathbf{I} \Rightarrow \mathbf{C}_S = S\mathbf{B}_{S_1} \qquad (18)$$

$$\Rightarrow \mathbf{T}_0 = D\mathbf{B}_D + S\mathbf{B}_{S_1} + R\mathbf{B}_R \qquad (19)$$

$$= \frac{1}{\sqrt{2}} \begin{bmatrix} D+S & -R \\ R & D-S \end{bmatrix}. \qquad (20)$$

---

[‡] The authors use a different $\tan^{-1}$ branch cut, giving $\theta \in [0, 2\pi)$.

Note that $\text{tr}(\mathbf{T}) = \sqrt{2}D$ and $\det(\mathbf{T}) = (D^2 - S^2 + R^2)/2$. Eigenvalues $\lambda_1$, $\lambda_2$ of $\mathbf{T}$ are roots of $\det(\mathbf{T} - \lambda\mathbf{I}) = \lambda^2 - \text{tr}(\mathbf{T})\lambda + \det(\mathbf{T})$. With

$$\Delta = S^2 - R^2, \qquad (21)$$

the quadratic formula, and some simplification, we find

$$\lambda_1 = \frac{D + \sqrt{\Delta}}{\sqrt{2}}; \ \lambda_2 = \frac{D - \sqrt{\Delta}}{\sqrt{2}}. \qquad (22)$$

The eigenvalues are complex conjugate when $|R| > S$ (rotation dominates stretching). While all these invariants are independent of $\alpha$, the eigenvectors $\mathbf{v}$ are oriented by $\mathbf{A}(\alpha)$:

$$\mathbf{v}_1 = \mathbf{A}(\alpha) \begin{bmatrix} R \\ S - \sqrt{\Delta} \end{bmatrix}; \ \mathbf{v}_2 = \mathbf{A}(\alpha) \begin{bmatrix} S - \sqrt{\Delta} \\ R \end{bmatrix}. \qquad (23)$$

These formulae can be verified by hand for the case $\alpha = 0$, and generalized by observing that if $\mathbf{v}_0$ is an eigenvector of $\mathbf{T}_0$ (20) with $\lambda\mathbf{v}_0 = \mathbf{T}_0\mathbf{v}_0$, then $\mathbf{A}(\alpha)\lambda\mathbf{v}_0 = \mathbf{A}(\alpha)\mathbf{T}_0\mathbf{v}_0 = \mathbf{A}(\alpha)\mathbf{T}_0\mathbf{A}(\alpha)^{\mathsf{t}}\mathbf{A}(\alpha)\mathbf{v}_0$ implies $\mathbf{A}(\alpha)\mathbf{v}_0$ is an eigenvector of $\mathbf{A}(\alpha)\mathbf{T}_0\mathbf{A}(\alpha)^{\mathsf{t}} = \mathbf{T}$, also with eigenvalue $\lambda$.

Relative to the $\gamma_d$, $\gamma_s$, $\gamma_r$ coordinates of Zhang et al. [ZYLL09, CPL*11], our $D$, $S$, $R$ coordinates are a $\sqrt{2}$ factor larger ($D = \sqrt{2}\gamma_d$, etc.). Their *eigenvalue manifold* is a spherical surface corresponding to the set $\{\gamma_d, \gamma_s, \gamma_r\}$ where $\gamma_d^2 + \gamma_s^2 + \gamma_r^2 = 1$ (and with the constraint that tensor orientation $\theta = 2\alpha = 0$). This is where $\|\mathbf{T}\|_F = \sqrt{D^2 + S^2 + R^2} = \sqrt{2}$. Zhang et al. parameterize the relationship between the $\mathbf{C}_R$ and $\mathbf{C}_S$ components with

$$\phi = \tan^{-1}(\gamma_r/\gamma_s) = \tan^{-1}(R/S) \qquad (24)$$

Angles $\phi \in [-\pi/2, \pi/2]$ and tensor orientation $\theta = 2\alpha \in [-\pi, \pi)$ parameterize, by spherical coordinates, a sphere they term the *eigenvector manifold*. This is exactly the sphere defined by $D = 0$ and $\|\mathbf{T}\|_F = \sqrt{2}$.

For characterizing the shape and orientation of flow when the Jacobian has complex eigenvalues ($|R| > S$), Zheng and Pang introduce *dual-eigenvectors* [ZP05]. Zhang et al. show [ZYLL09] that the dual eigenvectors of $\mathbf{T} = \mathbf{M}(D, S, R, \alpha)$ are the eigenvectors of

$$\mathbf{P}_T = \text{sgn}(R)S \begin{bmatrix} \cos(2\alpha + \frac{\pi}{2}) & \sin(2\alpha + \frac{\pi}{2}) \\ \sin(2\alpha + \frac{\pi}{2}) & -\cos(2\alpha + \frac{\pi}{2}) \end{bmatrix}. \qquad (25)$$

This statement of $\mathbf{P}_T$ uses our notation and drops a $\sqrt{2}$ factor unimportant for the eigenvectors. Following the simplification of (13) to (15) and using (16) we find:

$$\mathbf{P}_T = \text{sgn}(R)\, S\, \mathbf{A}(\alpha + \tfrac{\pi}{4})\mathbf{B}_{S_1}\mathbf{A}(\alpha + \tfrac{\pi}{4})^{\mathsf{t}} \qquad (26)$$

$$= \text{sgn}(R)\, S\, \mathbf{A}(\alpha)\mathbf{A}(\tfrac{\pi}{4})\mathbf{B}_{S_1}\mathbf{A}(-\tfrac{\pi}{4})\mathbf{A}(-\alpha) \qquad (27)$$

$$= \text{sgn}(R)\, S\, \mathbf{A}(\alpha)\mathbf{B}_{S_2}\mathbf{A}(\alpha)^{\mathsf{t}}. \qquad (28)$$

Eq. (26) affords a novel expression of the dual-eigenvectors $\mathbf{d}_1, \mathbf{d}_2$ of $\mathbf{T}$ as the columns of $\mathbf{A}(\alpha + \frac{\pi}{4}) = \mathbf{A}(\alpha)\mathbf{A}(\frac{\pi}{4})$:

$$\mathbf{d}_1 = \mathbf{A}(\alpha)\mathbf{A}(\tfrac{\pi}{4}) \begin{bmatrix} 1 \\ 0 \end{bmatrix} = \frac{\mathbf{A}(\alpha)}{\sqrt{2}} \begin{bmatrix} 1 \\ 1 \end{bmatrix} \qquad (29)$$

$$\mathbf{d}_2 = \mathbf{A}(\alpha)\mathbf{A}(\tfrac{\pi}{4}) \begin{bmatrix} 0 \\ 1 \end{bmatrix} = \frac{\mathbf{A}(\alpha)}{\sqrt{2}} \begin{bmatrix} -1 \\ 1 \end{bmatrix} \qquad (30)$$

Eq. (28) shows how $\mathbf{P}_T$ equals the anisotropic component $\mathbf{C}_S$ (15),

except for a $\text{sgn}(R)$ factor (determining whether $\mathbf{d}_1$ or $\mathbf{d}_2$ is the major eigenvector) and $\mathbf{B}_{S_2}$ replacing $\mathbf{B}_{S_1}$. We thus observe that dual-eigenvectors arise from a kind of *transpose* that swaps coordinates along the $\mathbf{B}_{S_2}$ and $\mathbf{B}_{S_1}$ basis matrices, while transpose normally swaps $\begin{bmatrix} 0 & 1 \\ 0 & 0 \end{bmatrix}$ and $\begin{bmatrix} 0 & 0 \\ 1 & 0 \end{bmatrix}$.

When $|R| > S$, Zhang et al. introduce *pseudoeigenvectors* as analogs to the eigenvectors when $|R| < S$ [ZYLL09]. In their notation, the pseudoeigenvectors of $\mathbf{T}(\theta, \phi)$ are the eigenvectors of $\mathbf{T}(\theta, \pi/2 - \phi)$ when $\phi > \pi/4$, and of $\mathbf{T}(\theta, {}^{-\pi}/2 - \phi)$ when $\phi < {}^{-\pi}/4$. From (24) we find:

$$\tan(\frac{\pi}{2} - \phi) = \tan(-\frac{\pi}{2} - \phi) = \frac{1}{\tan\phi} = \frac{1}{R/S} = \frac{S}{R} \qquad (31)$$

$$\Rightarrow \frac{\pm\pi}{2} - \phi = \tan^{-1}\frac{S}{R} = \tan^{-1}\frac{\text{sgn}(R)S}{|R|} \qquad (32)$$

and thus (in our notation) pseudoeigenvectors of $\mathbf{T} = \mathbf{M}(D, S, R, \alpha)$ are the eigenvectors of $\mathbf{M}(D, |R|, \text{sgn}(R)S, \alpha)$, i.e., swapping $S$ and $R$ while ensuring that the anisotropic coordinate $|R|$ remains positive and the sign of rotation coordinate is preserved. Our reformulation unifies the $\phi > \pi/4$ and $\phi < {}^{-\pi}/4$ cases, and clarifies that pseudoeigenvectors arise from a different kind of matrix transpose, one which swaps coordinates along the rotation $\mathbf{B}_R$ and stretching $\mathbf{A}(\alpha)\mathbf{B}_{S_1}\mathbf{A}(\alpha)^{\text{t}}$ directions of matrix space. This in turn provides a simple statement of the pseudo-eigenvectors of $\mathbf{T}$, based on (23):

$$\mathbf{p}_1 = \mathbf{A}(\alpha) \begin{bmatrix} \text{sgn}(R)S \\ |R| - \sqrt{-\Delta} \end{bmatrix}; \quad \mathbf{p}_2 = \mathbf{A}(\alpha) \begin{bmatrix} |R| - \sqrt{-\Delta} \\ \text{sgn}(R)S \end{bmatrix}. \qquad (33)$$

Like the eigenvectors and the dual-eigenvectors, the pseudoeigenvectors are oriented by $\mathbf{A}(\alpha)$, which rotates from the given $\mathbb{R}^2$ basis to the tensor orientation.

## 4. Glyph Design

### 4.1. Design Principles

We design our new tensor glyph according to methodical application of principles used previously for 3D symmetric tensor glyphs [SK10b], and generalized as algebraic visualization design principles [KS14]. Following the principle of Unambiguous Data Depiction, glyphs for very different tensors should be visually distinct. The Visual-Data Correspondence principle, stating that changes in the data should meaningfully correspond to changes in the visual representation, can be applied in at least three different ways. First, a notion of continuity arises from considering that two nearly equal tensors should be shown with glyphs that are visually very similar. We evaluate conformance to this principle by looking for large changes in the glyphs for tensors that densely sample paths through our design space. Second, glyphs should ideally have exactly the same symmetries as the underlying tensor: a transform that is a symmetry of the tensor (such as a rotation within the eigenspace of a repeated eigenvalue) should also be a symmetry of the glyph.

Third, transforms (such as negation or rotation) that significantly change a tensor, however, should be manifested as an analogous change in the glyph: the glyph for a rotated tensor should be the rotation of the glyph for the original tensor, and the glyph for a negated tensor should somehow appear as the "negation" of the

original tensor glyph. We use *transform legibility* to describe this aspect of visual-data correspondence. Though not stated as such, the superquadric glyphs in [SK10b] made negation legible with opponent colors (orange and blue) to show eigenvalue sign. Solid colors assigned to different regions of the eigenvalue manifold in [ZYLL09, CPL*11] exploit opponent colors to make legible the signs of rotation and scaling, though at the expense of continuity. Our glyph design uses transform legibility to assess how the glyphs change with negating $R$ and $D$.

The basic glyph formation equation from [SK10b] can be stated in terms of the mathematics of the previous section as:

$$G(\mathbf{T}) = s(\|\mathbf{T}\|_F) \, \tilde{\mathbf{E}} \, \tilde{\Lambda} \, \mathbf{b}(D, S, R). \qquad (34)$$

The base glyph geometry is $\mathbf{b}(D, S, R)$. The matrices $\tilde{\Lambda}$ and $\tilde{\mathbf{E}}$ are related to the eigenvalues and eigenvectors, respectively, of $\mathbf{T}$, though this relationship is more indirect in our new glyphs than with previous tensor glyphs. $s(\|\mathbf{T}\|_F)$ is some uniform scaling parameterized monotonically by the Frobenius norm (or "size") of $\mathbf{T}$. Our new glyphs contain as special cases the previously defined 2D superquadrics (transformed by the eigensystem) for symmetric tensors ($R = 0$) [SK10b], as well as the ellipsoids (transformed by the pseudoeigenvectors) for when $|R| > S$ [ZYLL09, CPL*11].

We are additionally guided in our glyph design by recognizing the asymmetric tensor as the Jacobian (first derivative) of some underlying vector field. The first-order Taylor expansion of a vector field $\mathbf{f}(\mathbf{x})$ is determined by the Jacobian $\nabla \mathbf{f}$ around a critical point $\mathbf{x}_0$ where $\mathbf{f}(\mathbf{x}_0) = \mathbf{0}$:

$$\mathbf{f}(\mathbf{x_0} + \varepsilon) \approx \nabla \mathbf{f}(\mathbf{x_0}) \, \varepsilon \qquad (35)$$

Topological flow analysis uses properties of $\nabla \mathbf{f}$ (a second-order tensor, not symmetric in general) at critical points to characterize the behavior of nearby streamlines [HH89, CPC90]. Conversely, given tensor $\mathbf{T}$, with (35) one can synthesize a flow field $\mathbf{v}(\mathbf{x})$ in which streamlines near $\mathbf{x} = \mathbf{0}$ visualize $\mathbf{T}$:

$$\mathbf{v}(\mathbf{x}) = \mathbf{T}\mathbf{x} \qquad (36)$$

Such streamlines guide the design of our tensor glyphs.

### 4.2. Choosing a Design Space

The four $(D, S, R, \alpha)$ coordinates completely describe the tensor (17), but we use the design principles above to reduce this to an intuitive two-dimensional space. First, we assert rotation legibility by making a glyph for a tensor $\mathbf{T} = \mathbf{M}(D, S, R, \alpha)$ be a rotation by $\mathbf{A}(\alpha)$ of the glyph for $\mathbf{M}(D, S, R, 0)$. To preserve rotational symmetry, however, the glyph should ideally be rotationally symmetric when $S = 0$, since the tensor only has meaningful orientation when $S > 0$ (17). We then assert scale legibility (34) by making the glyph for a tensor $\mathbf{T}$ with $\|\mathbf{T}\|_F \neq 1$ be a scaling by $s(\|\mathbf{T}\|_F)$ of the glyph for the tensor with $\|\mathbf{T}\|_F = 1$. This leaves a design space that is a scaling of the eigenvalue manifold [ZYLL09, CPL*11] by $1/\sqrt{2}$: the hemisphere defined by $\|\mathbf{T}\|_F = \sqrt{D^2 + S^2 + R^2} = 1$ and $S \geq 0$.

Noting that coordinates $D$ and $R$ have sign, we propose to exploit negation legibility for both. The glyph for $\mathbf{M}(D, S, R, 0)$ with dilation $D > 0$ should correspond to a visual "negation" of the glyph for $\mathbf{M}(-D, S, R, 0)$ with contraction $-D < 0$. The indication of $D$ must
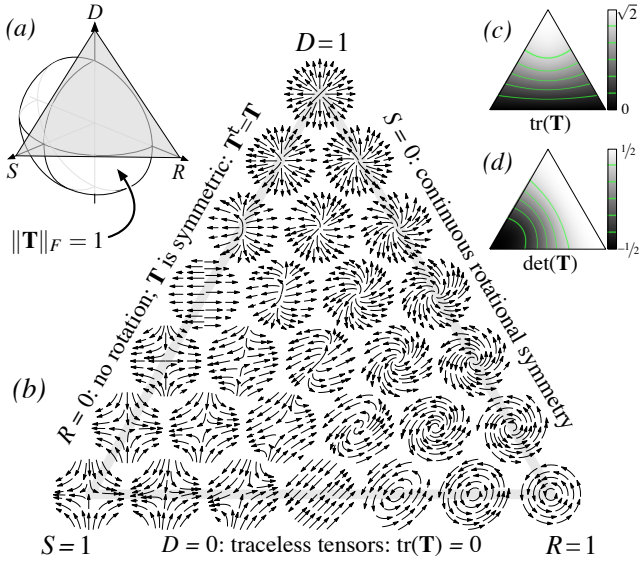
**Figure 1:** *Our glyph design space is the equilateral triangle formed by gnomonic projection of the* $\|\mathbf{T}\|_F = \sqrt{D^2 + S^2 + R^2} = 1$, $S \geq 0$, $D \geq 0$, $R \geq 0$, $\alpha = 0$ *portion of the tensor coordinates (a), shown with streamlines through* $\mathbf{v}(\mathbf{x}) = \mathbf{Tx}$ *(b) and maps of* $\text{tr}(\mathbf{T})$ *(c) and* $\det(\mathbf{T})$ *(d).*

smoothly vanish at $D = 0$ to ensure continuity. Rotation indicated by the glyph for $\mathbf{M}(D, S, R, 0)$ with $R > 0$ should likewise appear to be in the opposite direction of rotation indicated by the glyph for $\mathbf{M}(D, S, -R, 0)$, with all rotation indication smoothly vanishing at $R = 0$. This reduces the design space to the hemisphere quadrant $\|\mathbf{T}\|_F = \sqrt{D^2 + S^2 + R^2} = 1$, $D \geq 0$, $S \geq 0$, and $R \geq 0$.

Gnomonic projection (along lines through the origin, mapping great circles to straight lines), maps this quadrant to an equilateral triangle tangent to the hemisphere at $D = S = R = 1/\sqrt{3}$. Fig. 1(a) shows the hemisphere quadrant in question and the equilateral triangle tangent to it. Fig. 1(b) diagrams this triangle with streamline visualizations in the vector field generated by the tensor (36). The mapping from barycentric coordinates $(d, s, r)$ to tensor coordinates is $(D, S, R) = (d, s, r)/\sqrt{d^2 + s^2 + r^2}$. In Fig. 1(c), the trace $\text{tr}(\mathbf{T}) = \sqrt{2}D$ decreases from $\sqrt{2}$ at the top $D = 1$ corner to $\text{tr}(\mathbf{T}) = 0$ at the bottom $D = 0$ edge. Assuming the $\|\mathbf{T}\|_F = \sqrt{D^2 + S^2 + R^2} = 1$ restriction, from (20) we note

$$\det(\mathbf{T}) = \frac{D^2 - S^2 + R^2}{2} = \frac{1}{2} - S^2. \qquad (37)$$

$\det(\mathbf{T})$ is thus a function of $S$, varying in Fig. 1(d) from $\det(\mathbf{T}) = -1/2$ at the left $S = 1$ corner to $\det(\mathbf{T}) = 1/2$ along the right $S = 0$ edge. At the midpoints $S = D = 1/\sqrt{2}$ and $S = R = 1/\sqrt{2}$ of the left and bottom edges, $\det(\mathbf{T}) = 0$.

### 4.3. Glyphs at Triangle Edges

We first define glyphs for the three *edges* of the triangular design space (where the reduced degrees of freedom give more power to the design principles), and then fill the interior in a continuous way. Figures of the glyphs along the edges serve to qualitatively illus-

trate the design decisions, while the full mathematical definitions are given later, in Sec. 4.5

We start with the left $R = 0$ edge, where we copy previous superquadric glyphs for symmetric tensors [SK10b], as shown in Fig. 2. The base geometry is defined by [Bar81]:

$$\mathbf{b}(D, S, R) = (\cos^{a(D,S,R)} \theta, \sin^{a(D,S,R)} \theta); \quad 0 \leq \theta < 2\pi \qquad (38)$$

using signed exponentiation $x^a = \text{sgn}(x)|x|^a$; this $\theta$ has no relation to $\theta$ in [ZYLL09, CPL*11]. Eq. (34) creates the glyph from (38), with $\tilde{\Lambda}$ the diagonal matrix of eigenvalues of $\mathbf{T}$, and the eigenvectors of $\mathbf{T}$ in the columns of matrix $\tilde{\mathbf{E}}$. Superquadric tensor glyphs vary the shape parameter $a(D, S, R)$ according to the tensor coordinates. A detailed definition is below, but along this edge we note that $a$ varies smoothly from $a = 1$ at $D = 1$ to $a = 0$ at $D = 1/\sqrt{2}$ (gaining convex corners), jumps at $D = 1/\sqrt{2}$ to $a = 2$, and varies smoothly again to $a = 4$ at $D = 0$. The shape discontinuity is hidden by the zero eigenvalue scaling at $D = S = 1/\sqrt{2}$ where $\det(\mathbf{T}) = 0$. The $a = 1$ circle shape at $D = 1$ is the only choice that obeys the rotational symmetry of isotropic expansion. The glyph becomes more rotationally asymmetric as the tensor becomes more anisotropic ($|D|$ decreases), fitting how only the anisotropic component $\mathbf{C}_S$ carries tensor orientation. The coloring of the glyph is similar to that of [SK10b], which used the tensor contraction $\mathbf{x} \cdot \mathbf{Tx}$ between tensor $\mathbf{T}$ and unit direction $\mathbf{x}$. Rather than a solid coloring (with sharp edges) determined by the sign of $\mathbf{x} \cdot \mathbf{Tx}$, we choose opponent orange and blue hues for the extremum of $\mathbf{x} \cdot \mathbf{Tx}$, and blend with equiluminant gray at $\mathbf{x} \cdot \mathbf{Tx} = 0$. The invisibility of the glyph at $D = S$ (when compressed to a line) is addressed in previous work with a halo [SK10b], which we revisit below.

The right half of Fig. 2 shows something we believe has not been noted before in tensor glyph design: the concave outline of the superquadric glyph for $\mathbf{T}$ with $S > |D|$ mimics the hyperbolic shape of the streamlines of $\mathbf{v}(\mathbf{x}) = \mathbf{Tx}$ (36) (flowlines along gradients with constant Hessian $\mathbf{T}$). This became a principle that we sought to follow where possible in the remainder of the design space, especially for the traceless tensors along the bottom $D = 0$ edges of the design triangle, shown in Fig 3. Starting from pure deviatoric $(S, R) = (1, 0)$ tensors on left and moving right towards $S = R$, the eigenvectors $\mathbf{v}_1$ and $\mathbf{v}_2$ gradually become parallel (23) [ZYLL09, CPL*11]. We find that transforming the superquadric geometry by a matrix $\tilde{\mathbf{E}}$ with eigenvectors in its columns creates an outline that again mimics the hyperbolic shape of streamlines when $|R| < S$. When $|R| > S$, the pseudoeigenvectors (33) are instead in the columns of $\tilde{\mathbf{E}}$, following the finding by Zhang et al. that a circle transformed by the pseudoeigenvectors exactly attains the elliptical shape of the streamlines of $\mathbf{v}(\mathbf{x}) = \mathbf{Tx}$ [ZYLL09]. Throughout, we use the same coloring based on contraction $\mathbf{x} \cdot \mathbf{Tx}$, which yields gray at $R = 0$, where $\mathbf{Tx}$ is orthogonal (rotated 90 degrees) to $\mathbf{x}$. However, this
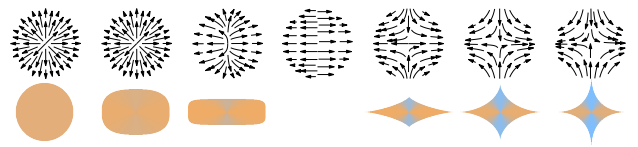


**Figure 2:** *Symmetric tensors going down left ($R = 0$) edge of triangle, from $(D, S) = (1, 0)$ (left) to $(D, S) = (0, 1)$ (right).*

produces a solid gray circle at $R = 1$, which conveys nothing of the rotation, which we address next.

Everywhere along the right $S = 0$ edge of the design space, tensors are invariant to rotation, so a circular shape is appropriate. This presents an interesting visualization design challenge: how does one indicate the direction and magnitude of a rotation in a rotationally symmetric way? The opponent coloring of [ZYLL09,CPL*11] shows only the largest differences in rotation (many similar tensors will receive the same color, violating the Unambiguity principle), and the assignment of red to counterclockwise and green to clockwise requires reference to a figure legend. Drawing inspiration from static depictions of motion blur, we propose the gradient pattern shown in Fig. 4, which roughly suggests four bright spokes rotating counterclockwise. The intensity gradient within each sector of the pattern indicates the direction and magnitude of the rotation component. This pattern also mimics the sawtooth luminance pattern that induces the peripheral drift illusion [FW79]. Viewed peripherally, one may perceive counterclockwise rotation in this pattern. Different repeating asymmetric luminance patterns eliciting the same illusion have been explored for flow and shape visualization [CLQW08, CYZL14]. Though we do not intend or require that our glyphs are viewed peripherally, the illusion gives additional evidence that the pattern can convey rotation. The gradients have opposite sense when $R < 0$. As the magnitude of the rotation component decreases, the contrast of the gradients fades to the hue determined by tensor contraction. The ramp pattern breaks the continuous rotational symmetry of the tensor itself at $S = 0$, but the number of discrete rotational symmetries can be increased with more sectors. We chose four sectors for our current work to maximize legibility of the rotation, at the expense of some rotational symmetry.

## 4.4. Glyphs at Triangle Interior

We now stitch together the glyph definitions along the triangle edges in a continuous and legible way to fill the interior. The first challenge is smoothly connecting the $|R| < S$ left side to the $|R| > S$ right side of the triangle, in which eigenvectors and pseudoeigenvectors, respectively, are the natural choice to fill the columns of $\bar{\mathbf{E}}$ (34).

Both eigenvectors and pseudoeigenvectors become parallel at $|R| = S$, however, so $\bar{\mathbf{E}}$ would become rank one, compressing the glyph to a line. While true to the mathematics, this violates continuity: isotropic ($D = 1$) tensors are shown with a circle, but arbitrarily close tensors with $|R| = S$ would be shown with a line.

We fix this by drawing on the geometric intuition that relates determinants with area. The determinant of $\mathbf{T}$ is the area of a unit square transformed by $\mathbf{T}$. Furthermore, if $\mathbf{T}$ is the Jacobian of a



**Figure 3:** *Traceless tensors going right along bottom ($D = 0$) edge, from $(S,R) = (1,0)$ (left) to $(S,R) = (0,1)$ (right).*
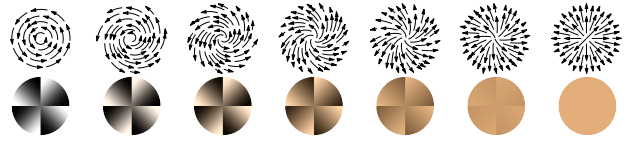


**Figure 4:** *Rotationally symmetry going up along right ($S = 0$) edge, from $(R,D) = (1,0)$ (left) to $(R,D) = (0,1)$ (right).*



**Figure 5:** *At $D = 0.9$, around $|R| = S$ glyphs shrink to an area unrelated to their determinant when their geometry is strictly determined by the (pseudo)eigenvectors (top row). Using quasi-eigenvectors (bottom row) fixes this.*

coordinate change, then the determinant of $\mathbf{T}$ is the infinitesimal element for area integrals. Using only (pseudo)eigenvectors creates near $|R| = S$ a glyph with misleadingly small area, given the determinant. Fig. 5 shows this by cutting across the design triangle near its $D = 1$ top. We define *quasi-eigenvectors* $\mathbf{q}_i$ below to give the glyph an area indicative of its determinant. Furthermore, the eigenvalues approach zero near $D = 0$ and $|R| = S$ (not shown), so we also define *quasi-eigenvalues* $\tilde{\lambda}_i$ to reflect the constant $\|\mathbf{T}\|_F$ within the design space.

Glyphs can also disappear when $\det(\mathbf{T}) = 0$, which we address with halos, as in previous work [SK10b]. Halos are created by drawing the glyph shape a second time with every vertex translated by a small amount along the normal to the glyph perimeter. The halo width is greatest at $S = \sqrt{D^2 + R^2} \Leftrightarrow \det(\mathbf{T}) = 0$ and decreases linearly to zero at $S = 0$ and $S = 1$. The halo appearance is determined by a similar gradient pattern as used to show rotation in the glyph interior.

## 4.5. Glyph Definition

Our full glyph definition for a given tensor $\mathbf{T}$ follows. First, we define the unit-norm $\mathbf{T}_1 = \mathbf{T}/\|\mathbf{T}\|_F$. The $(D,S,R,\alpha)$ coordinates of $\mathbf{T}_1$ are then found via (9) and (10). Then with (17) we define a tensor $\mathbf{T}'$ to unify the eigensystem and pseudoeigensystem computation.

$$\mathbf{T}' = \begin{cases} \mathbf{M}(D,S,R,\alpha) & |R| \leq S \\ \mathbf{M}(D,|R|,\text{sgn}(R)S,\alpha) & |R| > S \end{cases}. \quad (39)$$

Let $\lambda_1$, $\lambda_2$ be the eigenvalues and $\mathbf{v}'_1$, $\mathbf{v}'_2$ the eigenvectors of $\mathbf{T}'$, choosing the signs of $\mathbf{v}'_i$ to have a positive dot product with the major *dual* eigenvector $\mathbf{d}_1$ of $\mathbf{T}'$ (29). To prevent glyph shrinkage near $D = 0$ and $|R| = S$, for $i = 1,2$ let

$$\lambda'_i = \begin{cases} \lambda_i & |R| \leq S \\ 1 & |R| > S \end{cases}; \quad \tilde{\lambda}_i = \lambda'_i / \sqrt{\lambda'^2_1 + \lambda'^2_2}. \quad (40)$$

The quasi-eigenvalues $\tilde{\lambda}_i$ preserve relative magnitudes but not absolute values of $\lambda'_i$. To make the glyph area roughly indicate the tensor determinant, we compute the angle

$$\psi_d = \sin^{-1}\left(\frac{\det(\mathbf{T}')}{\tilde{\lambda}_1 \tilde{\lambda}_2}\right) \quad (41)$$

which gives the desired angle between scaled eigenvectors that would span a parallelogram of area $\det(\mathbf{T})$. This is compared with the actual angle between the eigenvectors

$$\psi_a = \cos^{-1}(\mathbf{v}_1' \cdot \mathbf{v}_2'). \tag{42}$$

If $\psi_a > \psi_d$, no adjustments to the eigenvectors $\mathbf{v}_i'$ are needed, and we set $\mathbf{q}_i = \mathbf{v}_i'$. Otherwise, we use the dual eigenvector basis $\mathbf{d}_1$ (29), $\mathbf{d}_2$ (30) to form quasi-eigenvectors $\mathbf{q}_i$ separated by angle $\psi_d$:

$$\mathbf{q}_1 = \cos(\psi_d/2)\mathbf{d}_1 + \sin(\psi_d/2)\mathbf{d}_2, \tag{43}$$

$$\mathbf{q}_2 = \cos(\psi_d/2)\mathbf{d}_1 - \sin(\psi_d/2)\mathbf{d}_2. \tag{44}$$

Glyphs are shaped and oriented via (34) with matrices

$$\tilde{\mathbf{E}} = \begin{bmatrix} \mathbf{q}_1 & \mathbf{q}_2 \end{bmatrix}, \ \tilde{\Lambda} = \begin{bmatrix} \tilde{\lambda}_1 & 0 \\ 0 & \tilde{\lambda}_2 \end{bmatrix}. \tag{45}$$

What remains is to define the base geometry and its coloring. The superquadric shape parameter $a(D, S, R)$ is defined to create circles when $|R| > S$, continuously blended with other convex shapes when $\det(\mathbf{T}) = 1/2 - S^2 > 0$, and concave shapes when $\det(\mathbf{T}) < 0$.

$$a(D, S, R) = \begin{cases} 1 & |R| > S \\ 4 - 2\sqrt{2}|D| & S > 1/\sqrt{2} \\ 1 - \sqrt{2}(S - |R|) & \text{otherwise} \end{cases} \tag{46}$$

The plot at left of the superquadric parameter $a(D, S, R)$ shows how it does not vary continuously over the design space, but the glyph shape being compressed to a line segment at $\det(\mathbf{T}) = 0$ hides the discontinuity there. The hue and saturation at position $\mathbf{x}$ relative to glyph center are determined by the expression $\mathbf{x} \cdot \mathbf{T}_1 \mathbf{x}$. In CIELAB color space we use $(L, A, B) = (80, 5.8\,\mathbf{x} \cdot \mathbf{T}_1 \mathbf{x}, 23.2\,\mathbf{x} \cdot \mathbf{T}_1 \mathbf{x})$ to generate orange and blue for positive and negative $\mathbf{x} \cdot \mathbf{T}_1 \mathbf{x}$, respectively. We implement negation legibility of $\mathbf{x} \cdot \mathbf{T}_1 \mathbf{x}$ by negation of CIELAB hue, with equi-luminant gray at $\mathbf{x} \cdot \mathbf{T}_1 \mathbf{x} = 0$.

Our principle for showing rotation with a gradient pattern inside the glyphs is that the gradient of the intensity ramp at some location $\mathbf{x}$ roughly indicates the vector $\mathbf{T}_1 \mathbf{x}$ (36): the rotation is towards higher intensities. For each of the four ramp sectors, let $\mathbf{c}$ be the vector from the glyph location to the areal center of the sector. The gray level intensity $L(\mathbf{x})$ at position $\mathbf{x}$ relative to glyph center is

$$\mathbf{r} = \mathbf{T}_1 \mathbf{c} - \frac{\mathbf{c} \cdot \mathbf{T}_1 \mathbf{c}}{|\mathbf{c}|}; \ L(\mathbf{x}) = (\mathbf{x} - \mathbf{c}) \cdot \mathbf{r} \tag{47}$$

To the extent that $\mathbf{T}_1$ exhibits rotation, $\mathbf{T}_1 \mathbf{c}$ has a tangential component $\mathbf{r}$ pointing in the rotation direction. The sector boundaries are oriented along the dual eigenvectors, which are stable except where $R = 0$ exactly. Finally, the glyphs are formed by (34), using the superquadric base geometry determined by (38) and (46), transformed by $\tilde{\mathbf{E}}$ and $\tilde{\Lambda}$ (45).

Halos are drawn around the transformed glyph geometry to ensure legibility even when the glyph interior is compressed to a line segment. The halos are filled with a similar ramp pattern as the glyph interior, except that the radial component of $\mathbf{T}_1 \mathbf{c}$ is not removed (because the halo must indicate all information about the underlying tensor when $\det(\mathbf{T}) = 0$): $L(\mathbf{x}) = (\mathbf{x} - \mathbf{c}) \cdot \mathbf{T}_1 \mathbf{c}$.
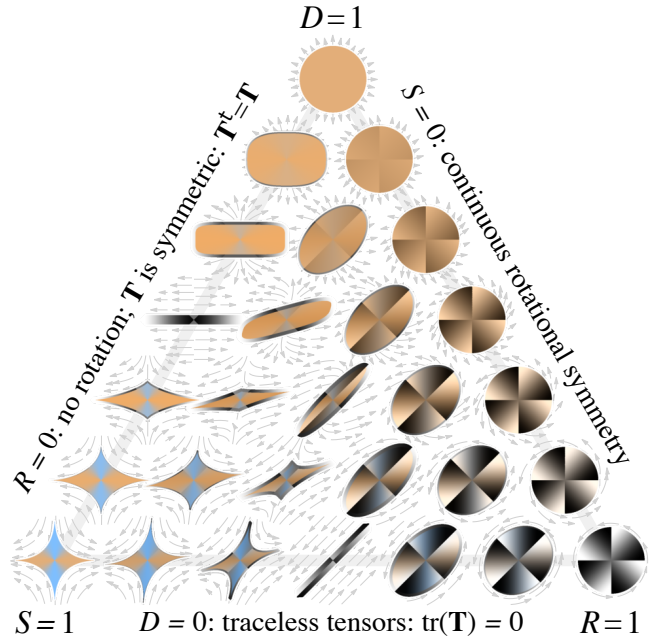
**Figure 6:** *Palette of our proposed tensor glyphs, shown over faint streamlines indicating the vector field created by (36).*
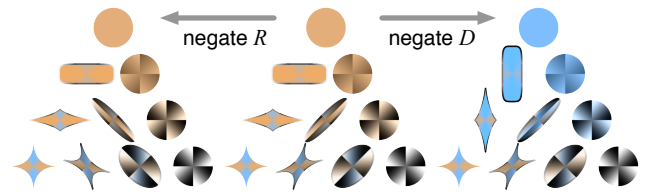


**Figure 7:** *Negation legibility is demonstrated by negating D (to the right, where blue shows contraction) and R (to the left, which reverses the rotation direction).*

Fig. 6 shows the final glyphs. The gradient pattern, showing the direction and magnitude of the rotation component, fades away towards the symmetric $R = 0$ case on the left edge. Non-circular glyph outlines indicate the amount and orientation of anisotropic stretching, blending to circles on the right $S = 0$ edge. On the exact $S = 0$ edge, the tensor is rotationally symmetric, so the orientation of the glyph is arbitrary (a shortcoming given the lack of continuous rotational symmetry in the gradient pattern there). Towards the $D = 0$ edge, the glyph outline conveys the shape of $\mathbf{Tx}$ streamlines, exactly matching them when $|R| > S$. The internal hue shows the sign of the stretching and isotropic components, fading to pure gray at the $R = 1$ corner. Halos preserve glyph visibility near $\det(\mathbf{T}) = 0$ while indicating rotation and stretching. Glyph continuity is preserved over the entire design space.

Fig. 7 demonstrates negation legibility with a coarse sampling of the design space. Negating $D$ has increasing effect moving towards the top $D = 1$ corner, and no effect at the bottom $D = 0$ edge. Negating $R$ has increasing effect towards the right $R = 1$ corner, with no effect on the left $R = 0$ edge. The relative subtlety of flipping gra-

dient pattern direction with *R* negation, versus the large hue change with *D* negation, highlights room for improvement in our design.

## 5. Results

We first apply our glyphs in Fig. 8, a 2D cross-section of a pair of superimposed Sullivan vortices (an exact solution of the Navier-Stokes equations [Sul59]). For the sake of comparison with results in [ZYLL09], we use the same vortex locations $(x, y) = (\pm 0.085, 0)$ and parameters: $a = 1.5$, $\Gamma = \pm 25$, $v = 0.1$. The 2D vector field records the $(x, y)$ vector components in the $z = 1$ plane. Fig. 8 shows our glyphs on a hexagonal grid, with glyph scaling $s(\|\mathbf{T}\|_F) = \|\mathbf{T}\|_F^{\frac{1}{4}}$. The contrast of the LIC background is modulated by the square root of vector magnitude. The full range of glyphs is visible. Regions of high vorticity ($|R|$ large relative to $|D|$ and $S$) appear on either side of the image center, where the gradient pattern is the dominant visual feature. Areas where $|D|$ is large stand out as highly saturated areas: convex orange glyphs show strong positive divergence at the center, while convex blue glyphs show negative divergence at the periphery. Areas characterized mainly by stretching ($S$ is large) are clearly indicated by concave superquadrics near the bottom of the image. The directions of expansion versus contraction are indicated by the blue versus orange glyph points.

There are several places where one eigenvalue is nearly zero, but the tensor is not near zero, so the glyph is visible mainly as a halo. The two glyphs indicated by white outlines in Fig. 8 are nearly rotations of each other: both indicate contraction in one direction. However, the glyph at the bottom shows contraction along the direction of flow (the gradients in the halo increase toward the
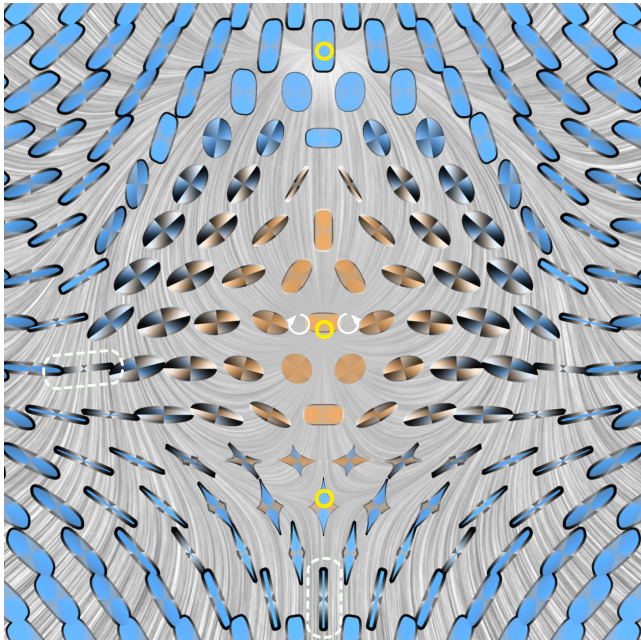
glyph center) and the glyph on the left shows contraction across the direction of flow.

There are three critical points in the flow, indicated by yellow circles. The bottom critical point is a saddle, identifiable by the concave glyph shape. The directions of the eigenvectors are aligned with the points of the glyph and the sign of the corresponding eigenvalue is indicated by hue. The glyph shape here matches the LIC texture in the same way as the glyphs and arrows match in Fig. 6. At the top and middle critical points, we see a sink and a source, respectively. The asymmetric glyph shapes clearly show that contraction and expansion are stronger in one direction than the other, which can also be seen in the LIC background. Near each of these points, the LIC texture approximates the arrows in Fig. 6.

Fig. 9 demonstrates our glyphs in a 2D flow (a central slice through a 3D unsteady flow simulation), using the same glyph scaling as the previous example. The image background is also LIC along streamlines, but with positive and negative vorticity indicated by magenta and green, respectively. The way the rotation alternates direction through the domain is unclear from the LIC alone. A particle system placed glyphs at vorticity extrema first, then spaced others out through the domain. One interesting feature of this visualization is that the glyphs in front of the obstacle show that the fluid is deformed by the obstacle, not significantly compressed. Our glyphs indicate that the Jacobian is quite large outside of the vortices, and that flow in those areas is dominated by deformation, rather than expansion or contraction. The directions of deformation are clearly seen, aligned with the points of the concave glyphs, and the directions of expansion and compression are indicated by hue.
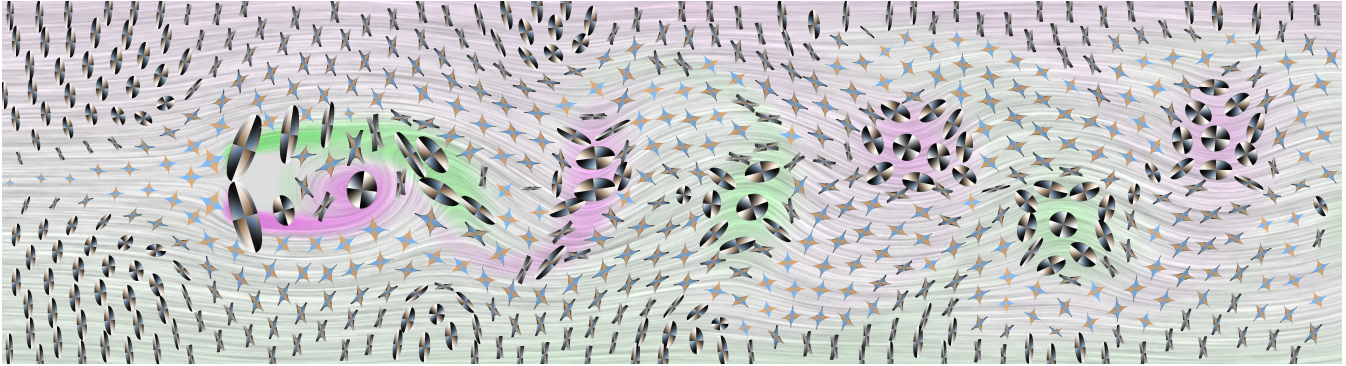
## 6. Conclusion

Our new glyph design effectively represents all asymmetric two-dimensional second-order tensors. Starting from precedent set by other work for visualizing tensors and tensor fields, we devised mathematical expressions that would preserve the intuitive correctness of those other designs and continuously deform to represent other tensors. The deformations chosen automatically respect the desired symmetry properties we were aiming for with respect to scaling and rotation. The class of $2 \times 2$ matrices may not seem like a significant visualization challenge, but it has remain unsolved. We also see significance in how our glyph was created largely by methodical and careful application of existing scientific visualization design principles, suggesting that they may soon be employed for more general problems.

More rigorous evaluation of our glyph design remains to be done. Good visualizations will in some way preserve the distances between objects being visualized [DSK*14]. Determining appropriate distance metrics for tensors, and for images of tensor glyphs, will take some care. Choosing such a metric and applying it to a large sampling of pairs of tensors and their glyph images would give a quantitative quality measure of our glyph design. If the glyphs are well designed, there should be a roughly linear relationship between the tensor distance and the glyph distance.

Ongoing work is expanding our design to 3D tensors. These can still be split into isotropic (one degree of freedom), anisotropic (five DOF), and antisymmetric (three DOF) parts. Both the anisotropic



**Figure 8:** *Two superimposed Sullivan vortices, shown with white arrows near center. Yellow circles indicate critical points. Two glyphs with a determinant close to zero are indicated by a white outline. The visualization domain is from $-1.125$ to $1.125$ in x and y.*

**Figure 9:** *Flow (from left to right) past a square obstacle creating a train of vortices.*

and antisymmetric parts carry information about orientation, but our gradient pattern may still have utility. Furthermore, the eigensystem analysis, a core part of our design, becomes more difficult, though recognizing that pseudo- and dual-eigenvectors arise from generalizations of tensor transpose may be helpful.

## Acknowledgements

## References

[AKK*13] AUER C., KASTEN J., KRATZ A., ZHANG E., HOTZ I.: Automatic, tensor-guided illustrative vector field visualization. In *Proc. PacificVis* (2013), pp. 265–272. 2

[Bar81] BARR A. H.: Superquadrics and angle-preserving transformations. *IEEE Comp. Graph. Appl. 1* (1981), 11–23. 5

[Bat67] BATCHELOR G. K.: *An introduction to fluid dynamics*. Cambridge university press, 1967, ch. 2. 2

[BML94] BASSER P. J., MATTIELLO J., LEBIHAN D.: MR diffusion tensor spectroscopy and imaging. *Biophysical Journal 66* (1994), 259–267. 2

[CLQW08] CHI M.-T., LEE T.-Y., QU Y., WONG T.-T.: Self-animating images: Illusory motion using repeated asymmetric patterns. *ACM Trans. Graphics 27* (Aug 2008). 6

[CPC90] CHONG M., PERRY A. E., CANTWELL B.: A general classification of three-dimensional flow fields. *Phys. Fluids A 2*, 5 (1990), 765–777. 4

[CPL*11] CHEN G., PALKE D., LIN Z., YEH H., VINCENT P., LARAMEE R. S., ZHANG E.: Asymmetric tensor field visualization for surfaces. *IEEE Trans. Vis. Comp. Graph. 17*, 12 (2011), 1979–1988. 1, 2, 3, 4, 5, 6

[CYZL14] CHI M.-T., YAO C.-Y., ZHANG E., LEE T.-Y.: Optical illusion shape texturing using repeated asymmetric patterns. *The Visual Computer 30* (2014), 809–819. 6

[DGBW09] DICK C., GEORGII J., BURGKART R., WESTERMANN R.: Stress tensor field visualization for implant planning in orthopedics. *IEEE Trans. Vis. Comp. Graph. 15*, 6 (2009), 1399–1406. 1, 2

[DH93] DELMARCELLE T., HESSELINK L.: Visualizing second-order tensor fields with hyperstreamlines. *IEEE Comp. Graph. Appl. 13*, 4 (1993), 25–33. 2

[dLvW93] DE LEEUW W. C., VAN WIJK J. J.: A probe for local flow field visualization. In *Proc. Vis.* (1993), pp. 39–45. 2

[DSK*14] DEMIRALP Ç., SCHEIDEGGER C. E., KINDLMANN G. L., LAIDLAW D. H., HEER J.: Visual embedding: A model for visualization. *IEEE Comp. Graph. Appl. 34* (2014), 10–15. 8

[FW79] FRASER A., WILCOX K. J.: Perception of illusory movement. *Nature 281* (1979), 565–566. 6

[Hab90] HABER R.: Visualization techniques for engineering mechanics. *Computing Systems in Engineering 1* (1990), 37–50. 2

[HFH*04] HOTZ I., FENG L., HAGEN H., HAMANN B., JOY K., JEREMIC B.: Physically based methods for tensor field visualization. In *Proc. Vis.* (2004), pp. 123–130. 1

[HH89] HELMAN J., HESSELINK L.: Representation and display of vector field topology in fluid flow data sets. *Computer 22*, 8 (1989), 27–36. 4

[HLL97] HESSELINK L., LEVY Y., LAVIN Y.: The topology of symmetric, second-order 3D tensor fields. *IEEE Trans. Vis. Comp. Graph. 3* (1997), 1–11. 2

[HYW03] HASHASH Y. M. A., YAO J. I.-C., WOTRING D. C.: Glyph and hyperstreamline representation of stress and strain tensors and material constitutive response. *Int. J. Numer. Anal. Methods Geomech. 27*, 7 (2003), 603–626. 2

[iCF] International CFD database. Formerly at http://cfd.cineca.it/. Further info at https://people.mpi-inf.mpg.de/~weinkauf/notes/squarecylinder.html. 9

[JSF*02] JEREMIĆ B., SCHEUERMANN G., FREY J., YANG Z., HAMANN B., JOY K. I., HAGEN H.: Tensor visualizations in computational geomechanics. *Int. J. Numer. Anal. Methods Geomech. 26*, 10 (2002), 925–944. 2

[KASH13] KRATZ A., AUER C., STOMMEL M., HOTZ I.: Visualization and analysis of second-order tensors: Moving beyond the symmetric positive-definite case. *Comp. Graph. Forum 32*, 1 (2013), 49–74. 1

[KS14] KINDLMANN G., SCHEIDEGGER C.: An algebraic process for visualization design. *IEEE Trans. Vis. Comp. Graph. 20* (2014), 2181–2190. 1, 4

[KWH00] KINDLMANN G., WEINSTEIN D., HART D.: Strategies for direct volume rendering of diffusion tensor fields. *IEEE Trans. Vis. Comp. Graph. 6*, 2 (2000), 124–138. 1

[LAK*98] LAIDLAW D., AHRENS E., KREMERS D., AVALOS M., JACOBS R., READHEAD C.: Visualizing diffusion tensor images of the mouse spinal cord. In *Proc. Vis.* (1998), pp. 127–134. 1

[LV12] LAIDLAW D., VILANOVA A. (Eds.): *New Developments in the Visualization and Processing of Tensor Fields*. Mathematics and Visualization. Springer Berlin Heidelberg, 2012. 1

[MSM95] MOORE J. G., SCHORN S. A., MOORE J.: Methods of classical mechanics applied to turbulence stresses in a tip leakage vortex. In *ASME International Gas Turbine and Aeroengine Congress and Exposition* (1995), pp. 622–629. 2

[NJP05] NEEMAN A., JEREMIC B., PANG A.: Visualizing tensor fields in geomechanics. In *Proc. Vis.* (2005), pp. 35–42. 2

[SEHW02] SIGFRIDSSON A., EBBERS T., HEIBERG E., WIGSTRÖM L.: Tensor field visualisation using adaptive filtering of noise fields combined with glyph rendering. In *Proc. Vis.* (2002), pp. 371–378. 2

[SK10a] SCHULTZ T., KINDLMANN G.: A maximum enhancing higher-order tensor glyph. *Comp. Graph. Forum 29*, 3 (2010), 1143–1152. 2

[SK10b] SCHULTZ T., KINDLMANN G.: Superquadric glyphs for symmetric second-order tensors. *IEEE Trans. Vis. Comp. Graph. 16*, 6 (2010), 1595–1604. 2, 4, 5, 6

[Sul59] SULLIVAN R. D.: A two-cell vortex solution of the navier-stokes equations. *J. Aerosp. Sci. 26*, 11 (1959), 767–768. 8

[TWHS03] THEISEL H., WEINKAUF T., HEGE H.-C., SEIDEL H.-P.: Saddle connectors - An approach to visualizing the topological skeleton of complex 3D vector fields. In *Proc. Vis.* (2003), pp. 225–232. 2

[WLW00] WIEGELL M. R., LARSSON H. B. W., WEDEEN V. J.: Fiber crossing in human brain depicted with diffusion tensor MR imaging. *Radiology 217*, 3 (2000), 897–903. 2

[WMK*99] WESTIN C.-F., MAIER S., KHIDHIR B., EVERETT P., JOLESZ F., KIKINIS R.: Image processing for diffusion tensor magnetic resonance imaging. In *Proc. MICCAI*. Springer, 1999, pp. 441–452. 2

[ZP03] ZHENG X., PANG A.: HyperLIC. In *Proc. Vis.* (2003), pp. 249–256. 1

[ZP05] ZHENG X., PANG A.: 2D asymmetric tensor analysis. In *Proc. Vis.* (2005), pp. 3–10. 1, 3

[ZYLL09] ZHANG E., YEH H., LIN Z., LARAMEE R. S.: Asymmetric tensor analysis for flow visualization. *IEEE Trans. Vis. Comp. Graph. 15*, 1 (2009), 106–122. 1, 2, 3, 4, 5, 6, 8